RESEARCH ARTICLE

QUANTUM SIMULATION

Observing the quantum topology of light

Jinfeng Deng[1]†, Hang Dong[1]†, Chuanyu Zhang[1], Yaozu Wu[1], Jiale Yuan[1], Xuhao Zhu[1], Feitong Jin[1], Hekang Li[1], Zhen Wang[1,2,3], Han Cai[1], Chao Song[1]*, H. Wang[1,2,3]*, J. Q. You[1], Da-Wei Wang[1,3,4]*

Topological photonics provides a powerful platform to explore topological physics beyond traditional electronic materials and shows promising applications in light transport and lasers. Classical degrees of freedom are routinely used to construct topological light modes in real or synthetic dimensions. Beyond the classical topology, the inherent quantum nature of light provides a wealth of fundamentally distinct topological states. Here we implement experiments on topological states of quantized light in a superconducting circuit, with which one- and two-dimensional Fock-state lattices are constructed. We realize rich topological physics including topological zero-energy states of the Su-Schrieffer-Heeger model, strain-induced pseudo-Landau levels, valley Hall effect, and Haldane chiral edge currents. Our study extends the topological states of light to the quantum regime, bridging topological phases of condensed-matter physics with circuit quantum electrodynamics, and offers a freedom in controlling the quantum states of multiple resonators.

The quantum Hall effect (*1*) reveals new phases of matter that are classified by the topological invariants of energy bands (*2*). For two-dimensional electrons in strong magnetic fields, the chiral edge states between Landau levels contribute to the quantized Hall conductivity, which is immune to local defects. This topological effect can also exist without Landau levels, such as in the Haldane model (*3*), which lays the basis for topological insulators (*4*). The optical simulation of quantum Hall edge states (*5*) opens a new research area, topological photonics (*6*–*8*), which brings a wealth of applications in routing and generating electromagnetic waves, such as backscattering-free waveguides (*9*) and topological insulator lasers (*10*). Classical degrees of freedom such as frequencies and orbital angular momenta have been widely used to synthesize new lattice dimensions to embed the topological modes (*11*–*13*). Such pure classical topology of light is in stark contrast to the topological phases of electrons, where the quantum wave and fermionic statistics play a fundamental role. Intriguingly, new topological states emerging from light quantization and bosonic statistics have been predicted beyond classical interpretation (*14*–*17*). Recent development in circuit quantum electrodynamics (QED) (*18*) makes it possible to realize these intrinsic quantum topological states of light, which provide quantum degrees of freedom in engineering photonic topology (*14*, *19*) and offer topological control knobs in bosonic quantum information processing (*20*–*23*).

Compared with lattices of modes in real or synthetic dimensions in classical topological photonics, the topological states of quantized light are embedded in lattices of Fock states $\Pi_i|n_i\rangle$ with n_i being the photon number in the ith mode. In the Fock-state lattice (FSL), a mode provides a dimension (*14*, *19*, *20*, *24*), in contrast to a site in traditional lattices, including those in synthetic dimensions (*11*–*13*, *25*). The FSLs exploit the infinite quantum Hilbert space of light, enabling the construction of high-dimensional lattices with only a few cavity modes. To sketch such dimensional scalability, we use the Jaynes-Cummings (JC) model (*26*), which describes the interaction between a two-level atom with quantized light. However, here we use multiple quantized light modes to couple the atom. With two light modes, the Fock states form one-dimensional (1D) lattices of the Su-Schrieffer-Heeger (SSH) model (Fig. 1A) (*27*). By adding just one other mode, we obtain two-dimensional (2D) strained honeycomb lattices (Fig. 1B) (*28*). These lattices are featured by site-dependent coupling strengths, which originate from the property of the bosonic annihilation operator a

$$a|n\rangle = \sqrt{n}|n-1\rangle \qquad (1)$$

For the vacuum state, $a|0\rangle = 0$, which leads to natural edges of FSLs when the photon number

[1]Interdisciplinary Center for Quantum Information, State Key Laboratory of Modern Optical Instrumentation, and Zhejiang Province Key Laboratory of Quantum Technology and Device, School of Physics, Zhejiang University, Hangzhou 310027, China. [2]Hangzhou Global Scientific and Technological Innovation Center, Zhejiang University, Hangzhou 311215, China. [3]Hefei National Laboratory, Hefei 230088, China. [4]CAS Center of Excellence in Topological Quantum Computation, Beijing 100190, China.
*Corresponding author. Email: chaosong@zju.edu.cn (C.S.); hhwang@zju.edu.cn (H.W.); dwwang@zju.edu.cn (D.-W.W.)
†These authors contributed equally to this work.

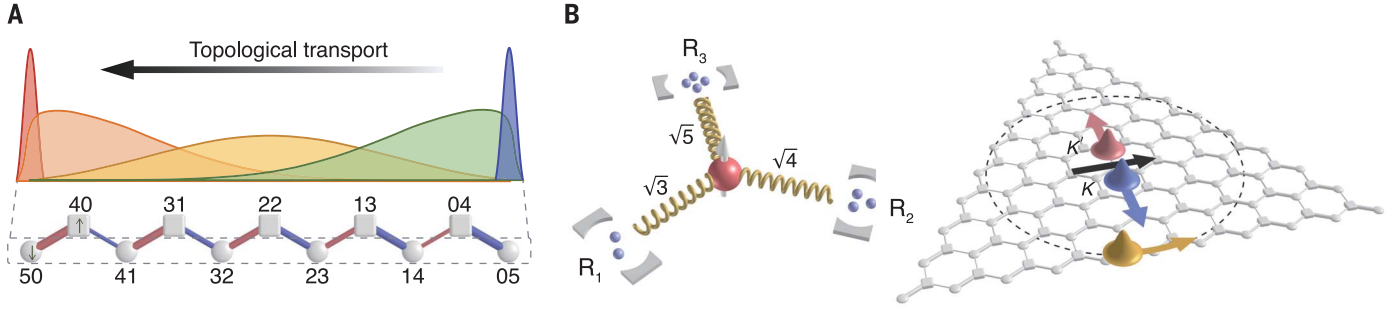

Fig. 1. Fock-state lattices of multimode Jaynes-Cummings models. (**A**) Topological transport of the zero-energy state of the SSH FSL with $N = 5$. The sublattice sites of $s = \uparrow (\downarrow)$ are denoted by squares (circles) and labeled by n_1n_2, the photon numbers in R_1 and R_2. The thicknesses of the lines connecting neighboring sites are proportional to the coupling strengths t_1 (red) and t_2 (blue). The wave function envelopes of four zero-energy states are schematically drawn with different colors. (**B**) The valley Hall response and the Haldane chiral edge state in a 2D FSL with $N = 10$. An excited qubit is coupled to three resonators with different photon numbers n_j (left). The coupling strengths are proportional to $\sqrt{n_j+1}$, which introduces competition between resonators to obtain a photon from the qubit. All the Fock states with the same N are coupled by the JC Hamiltonian to form a honeycomb lattice (right). The inhomogeneous coupling strengths induce an effective magnetic field in the 2D FSL. The VHE is featured by the wave packets at the two valleys moving in opposite directions perpendicular to an applied force (the black arrow). A Lifshitz topological edge (dashed line) separating the semimetallic and insulator phases locates on the incircle, which can host the Haldane chiral edge states (yellow wave packet with the arrow indicating the moving direction).

in one of the cavities reduces to zero. FSLs also have topological edges that host zero-energy states, resulting from the competition between resonators in exchanging photons with the atom. Such a simple mechanism enables FSLs to realize several important models in topological physics, in particular the seminal SSH and Haldane models, which have been the focus in various quantum platforms (*29*–*36*). Here we demonstrate adiabatic transport of topological zero-energy states in 1D SSH FSLs, where Fock states are topologically transferred from one cavity to another while maintaining the quantumness in superposition states. In 2D FSLs, we observe the valley Hall effect (VHE) (*37*) and the Haldane chiral edge current (*38*), which offer a topological route of engineering quantum states of multiple resonators.

Leveraging the advantageous integrability and tunability of the circuit QED platform (*39*–*42*), we design and fabricate a superconducting circuit to build and engineer the FSLs. The key elements of the circuit are a central gmon qubit (*43*) (Q_0) and three resonators (R_j with j running from 1 to 3), all with tunable frequencies. Each resonator R_j is coupled to Q_0 through an inductive coupler (C_j) (Fig. 2A). The coupling strengths $g_j/2\pi$ can be continuously tuned by changing the magnetic flux in C_j. In addition, each resonator R_j is capacitively coupled to an ancilla qubit Q_j for the preparation and readout of the resonator state. Other characteristics of the resonators and qubits can be found in the supplementary materials.

The Hamiltonian of the coupled system of R_j's and Q_0 can be described by a multimode JC model (*26*) in the rotating-wave approximation

$$H = \frac{\hbar\omega_0}{2}\sigma_z + \sum_{j=1}^{d}\hbar\omega_j a_j^\dagger a_j + \sum_{j=1}^{d}\hbar g_j\left(\sigma^+ a_j + a_j^\dagger\sigma^-\right) \quad (2)$$

where a_j is the annihilation operator of R_j with the transition frequency ω_j, $\sigma^+ \equiv |\uparrow\rangle\langle\downarrow|$ and $\sigma^- \equiv |\downarrow\rangle\langle\uparrow|$ are the raising and lowering operators

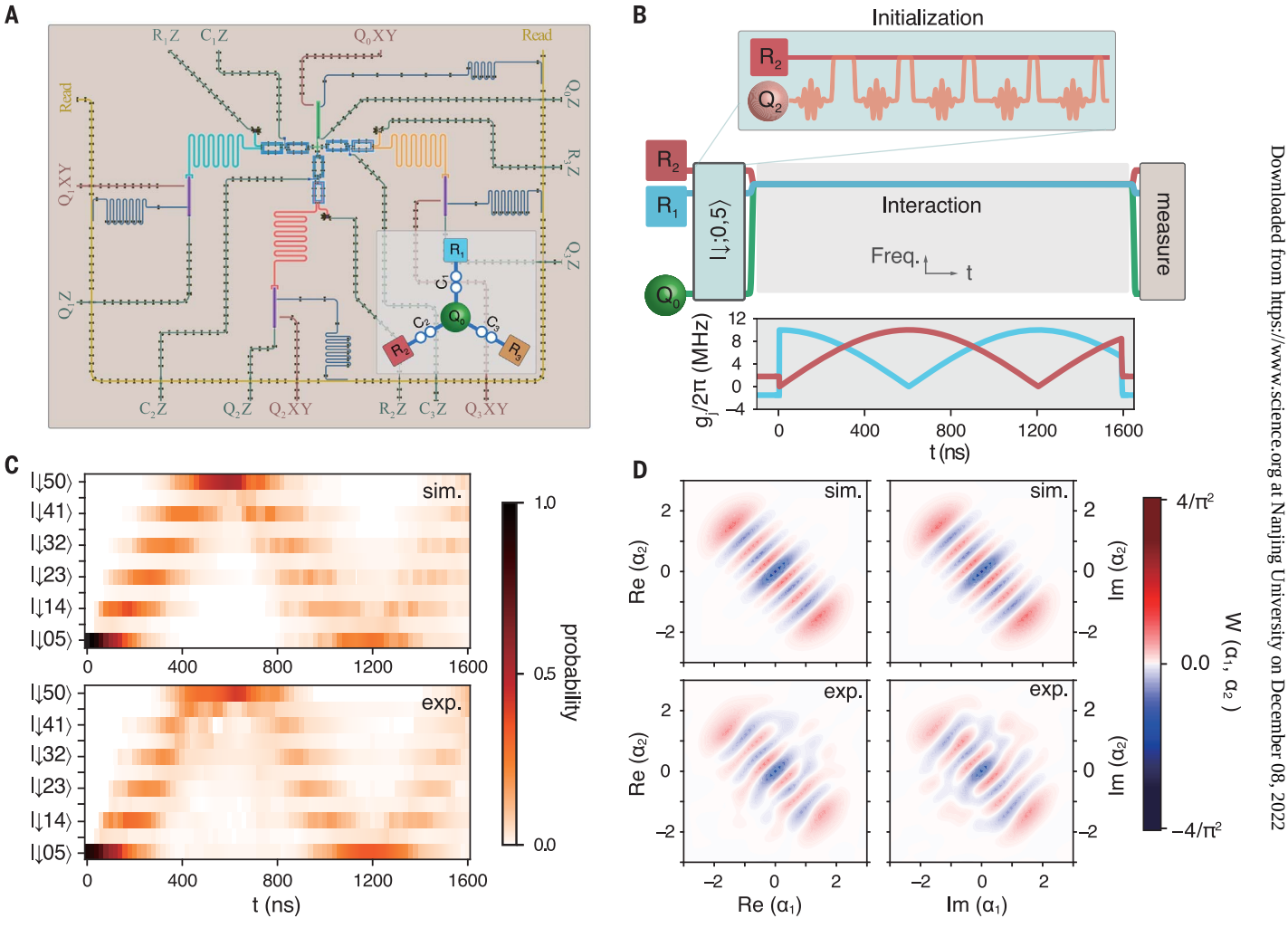

Fig. 2. Adiabatic transport of the topological zero-energy states in the Fock-state Su-Schrieffer-Heeger model. (**A**) False-color circuit image of the device of this experiment. Inset: Symbolized configuration of the key elements, a central gmon qubit Q_0 (green circle) coupled to three resonators (cyan, red and yellow squares for R_1, R_2, and R_3) via tunable couplers (blue twin circles). (**B**) Experimental pulse sequences for the adiabatic transport. We prepare the initial Fock state of R_2 by repeatedly exciting its ancilla qubit Q_2 with a π-pulse and tuning it in resonance with R_2 to swap the photons (upper panel). After the initialization, we tune R_1, R_2, and Q_0 in resonance (middle panel) and modulate C_1, C_2 to tune the coupling strengths g_1 (cyan line) and g_2 (red line) (lower panel). Finally, we measure the joint population of R_1, R_2, and Q_0. (**C**) The observed evolution of the zero-energy state wave packet in the numerical simulation (upper panel) and experiment (lower panel). Obviously $|\Psi_0\rangle$ only occupies the $|\downarrow\rangle$ sublattice. In numerical simulation, we use the parameters of the resonators and qubit listed in the table S1. All data in this paper, except that for quantum state tomography, are averaged over five runs of experiments. (**D**) The two-mode Wigner function of the resonator state at $t = 300$ ns in the plane-cut along axes Re(α_1)-Re(α_2) and Im(α_1)-Im(α_2), and the fidelity $F = 0.735$ (see fig. S6 for pulse sequence of tomography and more data at other times).

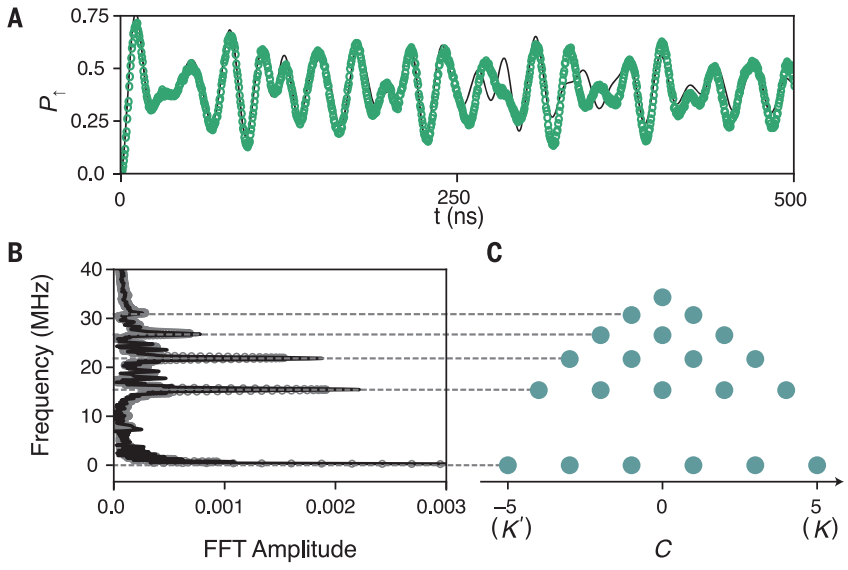

Fig. 3. The pseudo-Landau levels in the 2D Fock-state lattice with $N = 5$. (**A**) The evolution of the excited-state population of the qubit Q_0. (**B**) Fast Fourier transform of the Rabi oscillation. The vertical axis is the frequency component divided by 2. The solid line is the numerical simulation, and the circles are the experimental data. (**C**) The eigenstates in the zeroth and positive pseudo-Landau levels of the 2D FSL, with eigenenergies corresponding to the Fourier peaks. Each point labels an eigenstate characterized by the chirality C. The degeneracy of the nth Landau level is $N - n + 1$.

of Q_0 with the transition frequency ω_0, and d is the number of resonator modes. The Hamiltonian conserves the total excitation number $N = \sum_j n_j + (\sigma_z + 1)/2$, where n_j is the photon number of R_j and $\sigma_z = |\uparrow\rangle\langle\uparrow| - |\downarrow\rangle\langle\downarrow|$.

Topological transport

For $d = 2$ and N excitations, $2N + 1$ states $|s; n_1, n_2\rangle$ are coupled in a bipartite tight-binding lattices with the spin states $s = \uparrow, \downarrow$ labeling the two sublattices (Fig. 1A). When Q_0 is resonant with both resonators, all these $2N + 1$ states have the same energy, which is set as the zero energy. Because the coupling strengths $t_j = g_j\sqrt{n_j}$ $(j = 1, 2)$ depend on the photon numbers, $t_1 > t_2$ and $t_1 < t_2$ on the left- and right-hand sides of the FSL, resulting in two different topological phases of the SSH model (*27*). A topological zero-energy state locates around the lattice sites satisfying $t_1 = t_2$, which is the topological edge of the SSH model. We write $g_j = g_0\lambda_j$ where g_0 is a fixed nonzero coupling strength and λ_j's are the tunable parameters satisfying $\lambda_1^2 + \lambda_2^2 = 1$. The topological zero-energy state can be written as a two-mode binomial state (*14*, *44*)

$$|\Psi_0\rangle = \sum_{n=0}^{N} \sqrt{\frac{N!}{n!(N-n)!}} \lambda_2^n (-\lambda_1)^{N-n} \left|\downarrow; n, N-n\right\rangle \tag{3}$$

which only occupies the $|\downarrow\rangle$ sublattice. By adiabatically tuning λ_2 from 0 to 1, we can transport the topological zero-energy state from the right end of the lattice to the left end, or vice versa.

In the experiment we select R_1 and R_2 to construct the SSH FSL, with R_3 being far detuned and effectively decoupled from the system. In the experimental pulse sequences (Fig. 2B), we first prepare the initial state $|\downarrow; 0, 5\rangle$, which is the topological zero-energy state of the SSH FSL with $N = 5$ and $\lambda_1 = 1$, by pumping five photons successively into R_2 via Q_2 (upper panel of Fig. 2B). Then we tune R_1, R_2, and Q_0 in resonance at the frequency $\omega_{\text{int}}/2\pi \approx 4.81$ GHz and sinusoidally modulate the coupling strengths where $g_0/2\pi \approx 9$ MHz, $\lambda_1 = |\cos(2\pi\nu t)|$, and $\lambda_2 = |\sin(2\pi\nu t)|$ with $\nu = 416$ kHz $\ll g_0$ to satisfy the adiabatic condition (lower panel of Fig. 2B). Finally, the wave packet of the zero-energy state in the FSL is measured (see supplementary materials), with the data shown in Fig. 2C. The adiabatic transport of the topological edge state is witnessed by the oscillation of the photons between R_1 and R_2 following Eq. 3 with time-dependent λ_1 and λ_2. The zero-energy state is topologically protected by the energy gap g_0 from other eigenstates of the FSL and maintains coherence during the transport (*45*). To show this, we further measure the density matrix of the two resonators by quantum state tomography (Fig. 2D). The two-mode binomial state remains a Fock state in the combinational dark mode of the two resonators, $\lambda_2 a_1 - \lambda_1 a_2$, and the quantumness of the states is evident from the negative values of the two-mode Wigner functions.

Valley Hall effect

When $d = 3$, the Fock states in the subspace with N excitations form a two-dimensional honeycomb lattice containing $(N + 1)^2$ sites (Fig. 1B). The site-dependent coupling strengths introduce a strain, which has the effect of a magnetic field (*46*–*48*) and results in $\sqrt{n}$-scaling pseudo-Landau levels (*14*) when Q_0 is resonant with all three resonators. We observe the Landau levels by analyzing the spectra of the lattice dynamics (*49*). In the experiment, we prepare the initial state $|\downarrow; 0, 5, 0\rangle$ and resonantly couple R_1, R_2, and R_3 to Q_0 with coupling strengths $g_j/2\pi \approx 9$ MHz. We measure the evolution of the probability of finding Q_0 in the $|\uparrow\rangle$ state and then perform fast Fourier transform. We obtain peaks approximately located at $\sqrt{n}\Omega_0$ with $\Omega_0 = \sqrt{3}g_j$ (Fig. 3C). The degenerate states in the same Landau level are distinguished by their chiralities

$$C = b_+^\dagger b_+ - b_-^\dagger b_- \tag{4}$$

where $b_\pm = \sum_{j=1}^{3} a_j \exp(\mp i 2j\pi/3)/\sqrt{3}$ are the annihilation operators of the two chiral dark modes that are decoupled from the qubit. The chirality C plays the role of the lattice momentum in conventional lattices, and $C = N$ and $C = -N$ correspond to the two corners of the Brillouin zone, denoted as K and K' valleys, respectively (*14*, *50*).

A Lifshitz topological edge (*51*) on the incircle separates the FSL into two phases, a semimetallic phase within the incircle and a band insulator phase outside of it (see the dashed line in Fig. 1B). The states in the zeroth Landau level are confined within the incircle by an outside band gap of the insulator (*14*). In the semimetal, the strain-induced magnetic field has opposite signs at the K and K' valleys (see supplementary materials). By introducing a linear potential to mimic the effect of an electric field to electrons, we can observe the VHE (Fig. 1B); i.e., the Hall response has opposite signs at the two valleys. To experimentally demonstrate this effect, we first prepare an initial state $|\Psi_0\rangle$ with $\lambda_1 = \lambda_2 = 1/\sqrt{2}$ in Eq. 3 following the procedure in Fig. 2B. Such an initial state on the Lifshitz topological edge is a Gaussian wave function in the zeroth Landau level (*14*). Then we bring R_3 in resonance with Q_0 and set $g_j/2\pi \approx 9$ MHz for $j = 1, 2, 3$. The linear potential with horizontal gradient is introduced by slightly shifting the frequencies of R_1 and R_2

$$V = \hbar\delta\left(a_1^\dagger a_1 - a_2^\dagger a_2\right) \tag{5}$$

where the detuning $\delta/2\pi \approx 1.8$ MHz. We then measure populations on each lattice site and obtain the average photon numbers in the three resonators (Fig. 4B). The linear potential drives photons from R_1 and R_2 to R_3 whereas the qubit stays in the ground state. To visualize the evolution of the wave function, we draw the

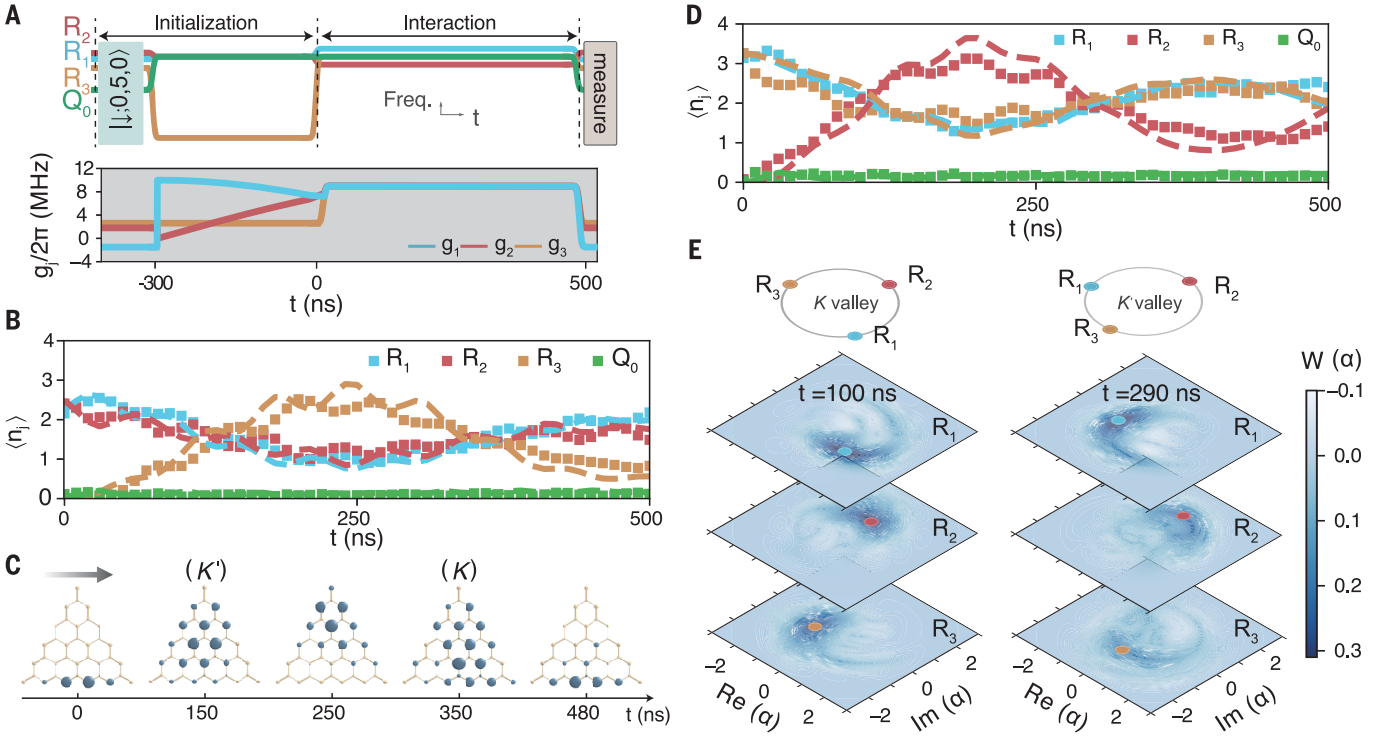

Fig. 4. The valley Hall effect in the 2D Fock-state lattice. (**A**) The pulse sequences for controlling the frequencies (upper panel) and coupling strengths (lower panel). We first prepare the initial state $|\Psi_0\rangle$ through the topological transport in the SSH FSL. Then we tune R_3 and Q_0 in resonance at $\omega_{int}/2\pi \approx 4.81$ GHz while we detune R_1 and R_2 to introduce the linear potential. Meanwhile we set the coupling strengths $g_j/2\pi \approx 9$ MHz for $j = 1, 2, 3$, and finally we measure the joint populations at different times during the evolution. (**B**) The valley Hall evolution of the average photon numbers in the three resonators for an initial two-mode binomial state $|\Psi_0\rangle$ with $N = 5$. The squares are experimental data, and the dashed lines are numerical simulations with the detuning $\delta/2\pi = 1.80$ MHz. (**C**) The populations in the FSL for N = 5 at t = 0, 150, 250, 350, and 480 ns. The left, right, and top vertices correspond to the states with all photons in R_1, R_2 and R_3. The radius of the blue circle on each site is proportional to its population. The trajectory of the wave function is perpendicular to the direction of the effective force (black arrow). (**D**) The evolution of the average photon numbers in the three resonators for the coherent initial state $|\Psi_c\rangle = |\downarrow;\alpha, 0, -\alpha\rangle$ with $\alpha \approx 1.8$. We detune R_1 and R_3 to introduce a linear potential $V = \hbar\delta\left(a_1^\dagger a_1 - a_3^\dagger a_3\right)$. In the numerical simulation (dashed lines), we set $\delta/2\pi = 2.35$ MHz. (**E**) The measured Wigner functions of the three resonator states at time t = 100 and 290 ns (see fig. S3 for the numerical simulation). The phases of the largest amplitudes of the Wigner functions are labeled on the unit circles, which show the chirality of the corresponding states in the two valleys.

population distributions in the FSL at five different times (Fig. 4C). The wave function first moves upward perpendicular to the force direction (black arrow) until being reflected by the Lifshitz topological edge near the top vertex, and then moves downward back to the initial state (up to a phase factor). In particular, when the wave function is at the center of the lattice but in different valleys—e.g., at $t = 150$ and 350 ns—it moves in opposite directions, which is a signature of the VHE (*14*). In contrast to the valley Hall effect in photonic lattices, where edges are routinely needed for the experimental implementation (*52*, *53*), here we coherently transport the quantum states to the two valleys and directly measure the valley Hall drift, thanks to the high tunability, controllability, and readability of the superconducting circuit. It is noteworthy that the qubit remains in the ground state during the evolution, which reflects a fundamental difference between classical and quantum predictions (fig. S5).

Surprisingly, the VHE can also be observed with initial classical states such as $|\Psi_c\rangle = |\downarrow;\alpha, 0, -\alpha\rangle$; i.e., R_1 and R_3 are in the coherent states $|\alpha\rangle$ and $|-\alpha\rangle$ and R_2 is in the vacuum state. This state can be expanded as a superposition of two-mode binomial states with different total excitation numbers N (*14*). Owing to the synchronized dynamics in different subspaces, the fields in the three resonators remain as a direct product of coherent states, and the evolution of the average photon numbers in the three resonators follows curves similar to that for an initial binomial state (Fig. 4D and supplementary materials).

The states in the two valleys are identified by their chiralities. Because the states of the three resonators are separable for coherent initial states, we perform simultaneous quantum state tomography and obtain their Wigner functions (Fig. 4E). As expected, the phases are distributed in a counterclockwise ($C > 0$) and clockwise ($C < 0$) manner at $t = 100$ and 290 ns when the wave function moves to the K and K' valleys, respectively. Therefore, the VHE in FSLs can be used to coherently transport the wave function between two valleys and control the chirality of the quantum states of multiple resonators.

Haldane model

By introducing a Floquet modulation of the coupling strength, $g_j(t) = g_0 + 2g_d\sin[\nu_d t + 2(j-1)\pi/3]$, we synthesize a most important model in topological physics, the Haldane model (*33*, *35*, *36*, *38*). The effective Hamiltonian in the second-order perturbation is (see supplementary materials)

$$H_H = \hbar g_0 \sum_{j=1}^{3}\left(a_j^\dagger \sigma_- + h.c.\right) + \hbar\kappa\sigma_z C \quad (6)$$

where $\kappa = -3g_d^2/\nu_d$. The second term in Eq. 6 introduces the complex next-nearest-neighbor hoppings in the FSL (*14*, *20*) and transforms flat Landau levels to a two-band structure with gapless chiral edge states, which originate from

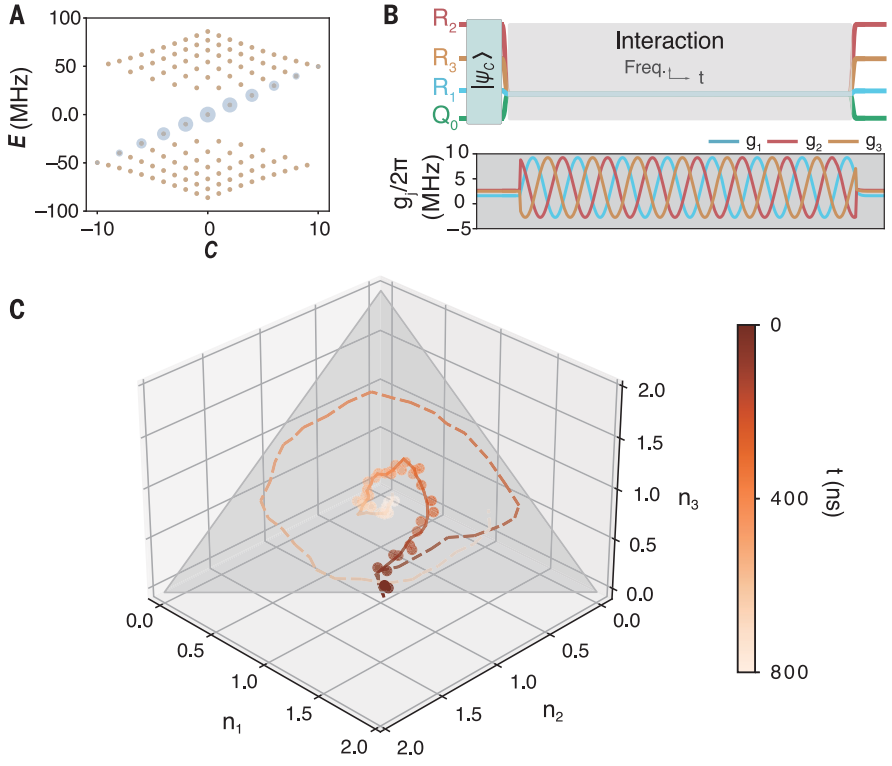

Fig. 5. Chiral edge currents of the Fock-state Haldane model. (**A**) The energy bands of the Hamiltonian H_H in Eq. 6 with total excitation number $N = 10$. The two energy bands are connected by chiral edge states, with each dot indicating an eigenstate. The populations of a binomial state (with $\lambda_1 = \lambda_2$) on the chiral edge states are proportional to the radii of the shaded circles. (**B**) The control sequence in realizing the Haldane Hamiltonian. We prepare an initial state $|\downarrow;\alpha,-\alpha,0\rangle$ with $\alpha \approx 1$ and tune three resonators and the gmon qubit on resonance at $\omega_{\text{int}}/2\pi \approx 4.82$ GHz, followed by a Floquet modulation of the coupling strengths $g_j(t)$ with static amplitude $g_0/2\pi \approx 2.5$ MHz, dynamic amplitude $g_d/2\pi \approx 3.25$ MHz, and modulation frequency $\nu_d/2\pi = 40$ MHz, such that the effective Haldane coupling strength $\kappa/2\pi = -0.79$ MHz. (**C**) Chiral edge currents shown by the average photon numbers in the three resonators. The total average photon number in the initial state is 2. The gray triangle shows the boundary of the FSL with $N = 2$, which is the most occupied subspace at the initial time. The circles show the experimental data, and the depths of the colors indicate the evolution time. Dashed lines are numerical simulations in the ideal case, whereas solid lines are those considering relevant parameter imperfections as described in the supplementary materials.

the zeroth Landau level (Fig. 5A). In the experiment, we directly excite R_1 and R_2 to obtain an initial state $|\downarrow;\alpha,-\alpha,0\rangle$ (see Fig. 5A for its distribution in the subspace $N = 10$). Then we periodically modulate the coupling strengths $g_j(t)$ to realize the Haldane Hamiltonian (see the control sequence in Fig. 5B). The average photon numbers are subsequently measured as a function of time (*17*), which shows the chiral motion; i.e., the wave function rotates in a counterclockwise manner in the FSL (Fig. 5C). Ideally the wave function shall be on the incircle, i.e., the Lifshitz topological edge. In the experiment, the chiral rotating wave function moves toward the center of the FSL owing to the decoherence and nonlinearity of the resonators, as well as the imperfect controlling pulses (figs. S8 to S11).

Concluding remarks

In this work, we have demonstrated the coherent control of topological zero-energy states in 1D and 2D FSLs. These states only occupy the sublattice where the qubit is in the $|\downarrow\rangle$ state, and they are protected from other eigenstates by an energy gap of the vacuum Rabi frequency. Perturbations with energy smaller than this gap, such as slow modulation of coupling strengths and small detunings between the resonators, are used to coherently control the zero-energy state to realize topological transport and VHE. Floquet modulations are introduced to realize the Haldane chiral edge currents. The techniques that we have developed in this study can also be applied to control other eigenstates in the FSL, such as the excited states in higher Landau levels. Our methods can be generalized to investigate topological states of more complex qubit-resonator coupled systems, where the number of resonators determines the dimension of the FSLs and each state of the qubits labels a sublattice, with richness beyond known topological phases in condensed-matter physics. Our study paves the way for investigating topological phases in FSLs and developing new control methods for quantum state engineering of bosonic modes.

REFERENCES AND NOTES

1. K. v. Klitzing, G. Dorda, M. Pepper, *Phys. Rev. Lett.* **45**, 494–497 (1980).
2. D. J. Thouless, M. Kohmoto, M. P. Nightingale, M. den Nijs, *Phys. Rev. Lett.* **49**, 405–408 (1982).
3. F. D. M. Haldane, *Phys. Rev. Lett.* **61**, 2015–2018 (1988).
4. C. L. Kane, E. J. Mele, *Phys. Rev. Lett.* **95**, 226801 (2005).
5. F. D. M. Haldane, S. Raghu, *Phys. Rev. Lett.* **100**, 013904 (2008).
6. L. Lu, J. D. Joannopoulos, M. Soljačić, *Nat. Photonics* **8**, 821–829 (2014).
7. A. B. Khanikaev, G. Shvets, *Nat. Photonics* **11**, 763–773 (2017).
8. T. Ozawa *et al.*, *Rev. Mod. Phys.* **91**, 015006 (2019).
9. Z. Wang, Y. Chong, J. D. Joannopoulos, M. Soljacić, *Nature* **461**, 772–775 (2009).
10. M. A. Bandres *et al.*, *Science* **359**, eaar4005 (2018).
11. L. Yuan, Q. Lin, M. Xiao, S. Fan, *Optica* **5**, 1396 (2018).
12. T. Ozawa, H. M. Price, *Nat. Rev. Phys.* **1**, 349–357 (2019).
13. E. Lustig, M. Segev, *Adv. Opt. Photonics* **13**, 426 (2021).
14. H. Cai, D.-W. Wang, *Natl. Sci. Rev.* **8**, nwaa196 (2020).
15. D. Cheng *et al.*, *Phys. Rev. Res.* **3**, 033069 (2021).
16. J. Mumford, Meissner effect in Fock space. arXiv:2208.01539 [quant-ph] (2022).
17. P. Saugmann, J. Larson, A Fock state lattice approach to quantum optics. arXiv:2203.13813 [quant-ph] (2022).
18. I. Carusotto *et al.*, *Nat. Phys.* **16**, 268–279 (2020).
19. J. Yuan *et al.*, *Phys. Rev. B* **104**, 035410 (2021).
20. D.-W. Wang, H. Cai, R.-B. Liu, M. O. Scully, *Phys. Rev. Lett.* **116**, 220502 (2016).
21. Y. Y. Gao *et al.*, *Nature* **566**, 509–512 (2019).
22. L. Hu *et al.*, *Nat. Phys.* **15**, 503–508 (2019).
23. W.-L. Ma *et al.*, *Sci. Bull.* **66**, 1789–1805 (2021).
24. J. Mumford, *Phys. Rev. A* **106**, 033317 (2022).
25. H. M. Price, T. Ozawa, N. Goldman, *Phys. Rev. A* **95**, 023607 (2017).
26. E. Jaynes, F. Cummings, *Proc. IEEE* **51**, 89–109 (1963).
27. W. P. Su, J. R. Schrieffer, A. J. Heeger, *Phys. Rev. Lett.* **42**, 1698–1701 (1979).
28. F. Guinea, M. I. Katsnelson, A. K. Geim, *Nat. Phys.* **6**, 30–33 (2010).
29. E. J. Meier, F. A. An, B. Gadway, *Nat. Commun.* **7**, 13986 (2016).
30. M. Kiczynski *et al.*, *Nature* **606**, 694–699 (2022).
31. O. Gröning *et al.*, *Nature* **560**, 209–213 (2018).
32. S. de Léséleuc *et al.*, *Science* **365**, 775–780 (2019).
33. G. Jotzu *et al.*, *Nature* **515**, 237–240 (2014).
34. P. Roushan *et al.*, *Nature* **515**, 241–244 (2014).
35. J. W. McIver *et al.*, *Nat. Phys.* **16**, 38–41 (2020).
36. W. Zhao *et al.*, Realization of the Haldane Chern insulator in a moiré lattice. arXiv:2207.02312 [cond-mat.mes-hall] (2022).
37. D. Xiao, W. Yao, Q. Niu, *Phys. Rev. Lett.* **99**, 236809 (2007).
38. M. C. Rechtsman *et al.*, *Nature* **496**, 196–200 (2013).
39. F. Arute *et al.*, *Nature* **574**, 505–510 (2019).
40. Y. Wu *et al.*, *Phys. Rev. Lett.* **127**, 180501 (2021).
41. D.-W. Wang *et al.*, *Nat. Phys.* **15**, 382–386 (2019).
42. W. Liu, W. Feng, W. Ren, D.-W. Wang, H. Wang, *Appl. Phys. Lett.* **116**, 114001 (2020).
43. P. Roushan *et al.*, *Nat. Phys.* **13**, 146–151 (2017).
44. H.-C. Fu, R. Sasaki, *J. Math. Phys.* **38**, 3968–3987 (1997).
45. J. Yuan, C. Xu, H. Cai, D.-W. Wang, *APL Photonics* **6**, 030803 (2021).
46. M. C. Rechtsman *et al.*, *Nat. Photonics* **7**, 153–158 (2013).
47. O. Jamadi *et al.*, *Light Sci. Appl.* **9**, 144 (2020).
48. M. Bellec, C. Poli, U. Kuhl, F. Mortessagne, H. Schomerus, *Light Sci. Appl.* **9**, 146 (2020).
49. P. Roushan *et al.*, *Science* **358**, 1175–1179 (2017).
50. A. H. Castro Neto, F. Guinea, N. M. R. Peres, K. S. Novoselov, A. K. Geim, *Rev. Mod. Phys.* **81**, 109–162 (2009).
51. M. O. Goerbig, *Rev. Mod. Phys.* **83**, 1193–1243 (2011).
52. G. Salerno, T. Ozawa, H. M. Price, I. Carusotto, *Phys. Rev. B* **95**, 245418 (2017).
53. F. Gao *et al.*, *Nat. Phys.* **14**, 140–144 (2018).
54. J. Deng, Observing the quantum topology of light [Data set], Zenodo (2022). https://doi.org/10.5281/zenodo.7267558.

ACKNOWLEDGMENTS

We thank K. Wang, W. Ren, J. Chen, and X. Zhang for technical support during the experiment. D.-W.W. is indebted to R. B. Liu

and C. Wu for inspiration, insightful discussion, and encouragement. The device was fabricated at the Micro-Nano Fabrication Center of Zhejiang University. **Funding:** We acknowledge the support of the National Key Research and Development Program of China (grant no. 2019YFA0308100), National Natural Science Foundation of China (grant nos. 11934011, 12174342, 92065204, U20A2076, and 11725419), the Zhejiang Province Key Research and Development Program (grant no. 2020C01019), the Fundamental Research Funds for the Zhejiang Provincial Universities (grant no. 2021XZZX003), and Innovation Program for Quantum Science and Technology (grant no. 2021ZD0303200). **Author contributions:** D.-W.W., C.S., and H. W. designed the experiment; J.D. and H.D. designed the device and carried out the experiments supervised by C.S. and H.W.; H.L. fabricated the device supervised by H.W.; J.D., C.Z., Y.W., and J.Y. performed the numerical simulations supervised by C.S. and D.-W.W.; J.D., C.S., and D.-W.W. wrote the manuscript with comments and inputs from other authors. All authors contributed to the analysis of data and the discussions of the results. **Competing interests:** All authors declare no competing interests. **Data and materials availability:** The data presented in the figures and that support the other findings of this study are available at Zenodo (*54*). **License information:** Copyright © 2022 the authors, some rights reserved; exclusive licensee American Association for the Advancement of Science. No claim to original US government works. https://www.science.org/about/science-licenses-journal-article-reuse

SUPPLEMENTARY MATERIALS

science.org/doi/10.1126/science.ade6219
Supplementary Text
Figs. S1 to S11
Table S1
References (*55*–*61*)

Submitted 28 August 2022; accepted 4 November 2022
10.1126/science.ade6219

Observing the quantum topology of light

Jinfeng DengHang DongChuanyu ZhangYaozu WuJiale YuanXuhao ZhuFeitong JinHekang LiZhen WangHan CaiChao SongH. WangJ. Q. YouDa-Wei Wang

Science, 378 (6623), • DOI: 10.1126/science.ade6219

Topological quantum photonics

Exploiting the topological properties of materials is expected to provide a route to developing robust platforms for transport and communication systems that are immune to defects. In optics, the demonstration of topological behavior has been confined mainly to classical light. Deng *et al*. introduce a superconducting chip–based platform consisting of a single qubit coupled to a number of resonators. By controlling the photon population in each resonator and the coupling strength, the authors were able to realize several important models in topological physics. The approach bridges the gap between topological states of classical and quantum origin. —ISO